Effect of Particle Size on the Adsorption and Desorption Properties of Oxide Nanoparticles

Hao Wang and Farhang Shadman
Chemical and Environmental Engineering Dept., University of Arizona, Tucson, AZ 85721

DOI 10.1002/aic.13936
Published online December 3, 2012 in Wiley Online Library (wileyonlinelibrary.com).

Using water molecules as a model adsorbing compound, the effect of particle size on the adsorption and desorption properties of porous oxide nanoparticles (NPs) was investigated at different temperatures. The moisture concentration on the surface of NPs was measured by monitoring the infrared spectra peaks corresponding to the stretching vibration of water molecules. A transient multilayer model was developed to represent the fundamental steps in the process. The thermal stability of adsorbed species and the strength of bonding to the surface were evaluated by determining the activation energies of various steps. The results indicate that the surface interaction parameters are both temperature and particle-size-dependent. Smaller NPs have a higher saturated surface concentration and a slower response to purging and desorption. As temperature decreases, NPs exhibit a higher saturated moisture concentration and are more prone to the adsorption of moisture and similar contaminants.
 AIChE J, 59: 1502–1510, 2013
Keywords: nanoparticle, adsorption/outgassing, process modeling, materials, surface activity

Introduction

The environmental safety and health (ESH) impact of nanoparticles (NPs) used in various industries and products has received a great deal of attention in recent years, however the mechanisms causing the ESH impact of NPs are not yet well understood. The unique chemical and physical characteristics of nanomaterial make it challenging to study their biological interactions accurately and reproducibly. The influence of physicochemical factors such as geometry, pore size, and surface functional groups of NPs are very critical for successful application of nanomaterial.[1] As an example, porosity and surface functionality of nanoparticles are critical factors that could affect the interaction of silica nanoparticles with biological systems.[2–4] The pore size of SiO_2 is a key factor in determining the adsorption capacity of proteins such as bovine serum albumin, where the adsorption capacity was elevated as the pore size of SiO_2 increased.[3] The intrinsic ability of NPs to traverse cell membranes might not be the primary reason for toxicity. The more critical factor appears to be the physicochemical properties such as the high-specific surface area, highly reactive surface sites, and the tendency to adsorb and retain other toxic chemicals. In general, these physicochemical properties of NPs could raise the toxicity of NPs.

The adsorption of various adsorbates on microporous adsorbents using Fourier transform infrared (FTIR) spectroscopy has been the subject of a number of previous studies. Infrared absorption introduced by molecule rotational and vibrational movements has been used in studying the physisorbed and chemisorbed species on a certain adsorbent surface.[5] Usually, FTIR spectroscopy is used to study the molecule's behavior qualitatively. However, FTIR could be an effective tool for quantitative measurements of molecule adsorption. By measuring absorbance of the corresponding IR peaks, the kinetic study of diffusion and counterdiffusion in zeolites has been proposed by IR spectroscopy.[6] FTIR has also been used to study the adsorption of water on ZSM-5 zeolites.[7] The success of FTIR technology is due to the well-documented spectral nature of the adsorption of these sorbates. CO_2 and H_2O are considered to be useful probe molecules for studying the structural features of a microporous sorbent.[8]

A previous study on water adsorption and desorption on various surfaces was carried out at different temperatures. Dillon et al. studied the mechanism of H_2O decomposition from 300 K to 860 K.[9] This study indicated that SiOH species decomposed to form a silicon oxide species and generated additional surface hydrogen between 460 K and 580 K. When the temperature is above 700 K, the SiH surface species decreased as H_2 desorption from the silicon surface. However, this study was not aimed at, nor did it provide information on the dynamics and kinetics properties of adsorption and desorption processes.

The objective of our research is to investigate the surface characteristics of oxide NPs, particularly silica, hafnia and ceria, which are used in semiconductor manufacturing. In particular, the focus of the study is on the surface properties that affect the adsorption and desorption of gaseous compounds on the surface of the particles. In our previous work, we verified the species and size effect on the NP surface properities and it only indicated the size effect on HfO_2 with the sizes of 20 nm and 100 nm. Our current research is focusing on the particle size effect on adsorption and

Correspondence concerning this article should be addressed to F. Shadman at shadman@erc.arizona.edu.

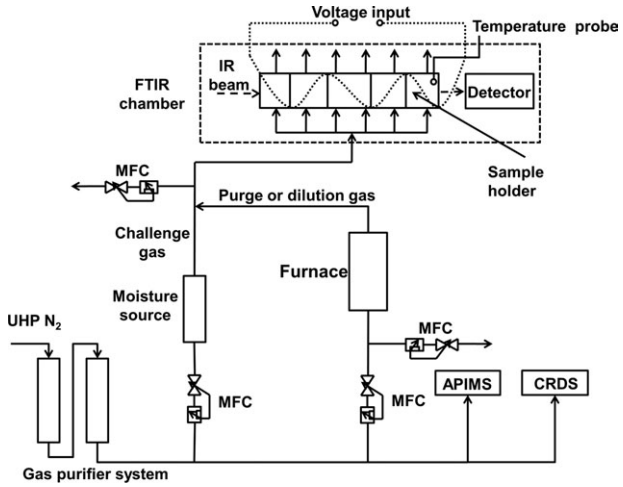

Figure 1. Schematic diagram of the experimental setup.

desorption properties of various oxide NPs such as SiO_2 (20 nm, 80 nm), HfO_2 (20 nm, 100 nm), and CeO_2 (20 nm, 50 nm) at different temperatures (25°C, 55°C, 80°C and 105°C). The experimental setup has been upgraded with a temperature control system to control the temperature inside of the sample cell. The process model has also been extended to simulate the adsorption and desorption prcess on one single NP including the porosity of the particles. Two different domains of transport have been considered, and each one has its own conservation formulation; this means two independent coordinate systems. The effect of temperature has also been studied and presented. In the following section, these will be discussed in detail.

Experimental Method

An experimental setup was designed and fabricated for studying the surface properties of NPs using a dynamic adsorption and desorption profiling technique. Since the physical and chemical interactions of moisture with the surfaces of interest could determine various types of surface sites and the IR spectra feature of adsorbed H_2O is well-documented, moisture was used as the characterizing adsorbate in this study. The method and most of the comparative conclusions would be valid for other similar sorbates when comparing NPs of different materials and sizes at different temperatures. The unique aspect of the experimental technique is the measurement of both surface and gas-phase concentrations of adsorbate simultaneously, and the effect of the gas phase moisture was eliminated in the later study.[10] Atmospheric pressure ionization mass spectrometer (APIMS), and cavity ring-down spectrometer (CRDS), were used for measuring the concentration of contamination in the background gas phase. The moisture background of purge gas is below 5 ppb (parts per billion). A stainless steel cell was designed and integrated into an FTIR spectrometer for direct measurement of the surface concentration. The sample cell was equipped with heating elements, insulated walls, and a temperature probe providing a uniform and steady operation in high-temperature experiments. The thermal probe output was used to control the heating element input for temperature control.

The experimental setup in Figure 1 consists of three sections: the gas mixing section, the customized sample cell, and the FTIR analyzer. In the gas mixing section, an ultra high purity (UHP) nitrogen gas flows through two purifiers to maintain moisture concentration below 5 ppb level. The UHP N_2 gas splits into two lines: a challenge gas line, and a purge-flow line. Nitrogen gas is controlled by a mass-flow controller (MFC) in the challenge line, and gas flow goes through an ultra-pure water bubbler. Based on dilution gas flow rates, this bubbler could generate a certain concentration of moisture in the ppm (parts per million) level. To assure experimental reproducibility, the purge flow line is heated up to 200°C. The sample cell is also purged with high-temperature UHP N_2 to fully clean out any residual moisture on the NP sample and the cell surfaces before each experiment. When the moisture absorption peak reaches the baseline in the FTIR spectra, this initial cleaning and purging would be stopped.

The experimental procedure had two stages: the challenge (adsorption) process, and the purge (desorption) process. In the challenge stage, the NP sample was exposed to a certain concentration of moisture carried by the UHP N_2 gas; the flow rate and temperature were controlled by the MFC and the input voltage, respectively. When the sample reached saturation, the gas flow was switched to UHP N_2 to initiate the desorption stage. For temperature effect studies, a similar challenge-purge procedure was repeated, using the same challenge concentration but different temperatures. Before the adsorption stage, a clean background scan was taken by the FTIR, eliminating the disturbance of the system background. During the desorption stages, FTIR scans were taken at regular intervals. The spectrum of the introduced moisture was recorded to monitor the temporal change of IR intensity at certain wave numbers corresponding to moisture vibrational frequency. The high-broad absorption peak from 3,500 cm^{-1} to 2,700 cm^{-1} was used to measure the moisture concentration on the NP surfaces.

Inside the FTIR chamber, an infrared (IR) beam passed through a custom-made stainless steel sample cell which contained a Teflon coupon with small indentations that contained the NPs. The IR beam passed through windows on both sides of the sample cell. The sealed sample cell had an inlet and an outlet allowing a controlled flow of purge gas. Since the pressure inside the cell was kept slightly higher than the pressure outside the cell by flow of challenge and purge gases, it prevented any leakage of impurities coming into the cell. Another UHP N_2 gas line kept purging the FTIR chamber itself during the entire process. The direction of challenge or purge gas flow was tangential to the coupon surface to allow gas transport while avoiding any movement and loss of particles.

The NPs were randomly packed in the columns inside of the packed-bed and were placed in the path of the IR beam inside the sample cell. The loose random packing of NPs did not change the surface characteristic of the particles or their fundamental adsorption and desorption characteristics in the gas phase. Moreover, the data analysis method, presented in the next section, allowed extraction of single-particle surface information from the FTIR measurements of the packed samples.

SiO_2 samples 20 nm and 80 nm were purchased from Sigma Aldrich and Nanostructured and Amorphous Materials, respectively. The specific surface areas are 590–690 m^2/g and 440 m^2/g, respectively. The density of SiO_2 samples are between 2.2 g/cm^3 and 2.6 g/cm^3 at 25°C. CeO_2 samples 20 nm and 50 nm were purchased from Sigma Aldrich. The specific surface areas for CeO_2 50 nm is

30 m^2/g. The density of CeO_2 samples are 7.13 g/cm^3 at 25°C. HfO_2 samples 20 nm and 100 nm were manufactured by Sematech and American Elements, respectively. The specific surface area for HfO_2 100 nm is in the range of 25–50 m^2/g. The density of HfO_2 samples are 9.68 g/cm^3.

Process Model

A process model was developed to elucidate the dynamics of multilayer transient interactions of an adsorbate with the NPs. The model assumes uniform surface properties, porosity, and an equivalent spherical shape for particles. The model simulated the process in two domains: One is the domain of a single particle; this domain has an r-axis, where r represents the position along the radius of one NP. The other domain is that of the packed-bed of NPs with x as the coordinate along the depth of the bed. The two domains are linked through the boundary conditions for the particles.

Single-particle domain

In the NP domain, the rates of adsorption and desorption follow the standard elementary reaction format in which the reaction rate is proportional to the concentration of reactants and a temperature-dependent rate coefficient. All adsorption and desorption reactions proposed in this model are assumed to be reversible. The adsorption and desorption rates are given by

$$r_a = k_a(S_0 - C_{s_{in}})C_{g_{in}}, \tag{1}$$

$$r_d = k_d C_{s_{in}}, \tag{2}$$

where k_a and k_d are adsorption and desorption rate coefficient, respectively, $C_{g_{in}}$ is the moisture concentration in the gas phase inside of the NP domain $C_{s_{in}}$ is the moisture concentration on the total adsorbed surface inside of the NP domain, and S_0 is the maximum capacity of the surface at certain challenge concentration.

The current multilayer model assumes the presence of two types of adsorption. One type is called chemisorption which is driven by chemical reaction occurring on the exposed surface; it has a strong interaction between the adsorbate and the substrate surface and creates new types of electronic bonds. The other type is called physisorption which forms a weak bonding due to the induced dipole moment of nonpolar adsorbate interacting with its own image charge in the polarizable solid.[11] During the challenge phase, water molecules chemisorb on the surface of the substrate and form new available sites for physisorption; water molecules then accumulate on the substrate surface and form multiple layers. The total number of layers is related to the the maximum capacity of the surface and the challenge concentration. The maximum capacity of the surface is the sum of the available sites on the substrate surface and the available sites formed by adsorbed water molecules. Therefore, the total available sites may vary with different challenge concentrations.

The rate coefficient follows the form of a prefactor multiplied by an exponential factor, which is presented as follows

$$k_a = k_{a_0} \exp\left(\frac{-E_a}{RT}\right), \tag{3}$$

$$k_d = k_{d_0} \exp\left(\frac{-E_d}{RT}\right), \tag{4}$$

where k_{a_0} and k_{d_0} are the prefactors for adsorption and desorption rate coefficients, E_a is the total adsorption energy, E_d is the total desorption energy, R is the gas constant, and T is the temperature.

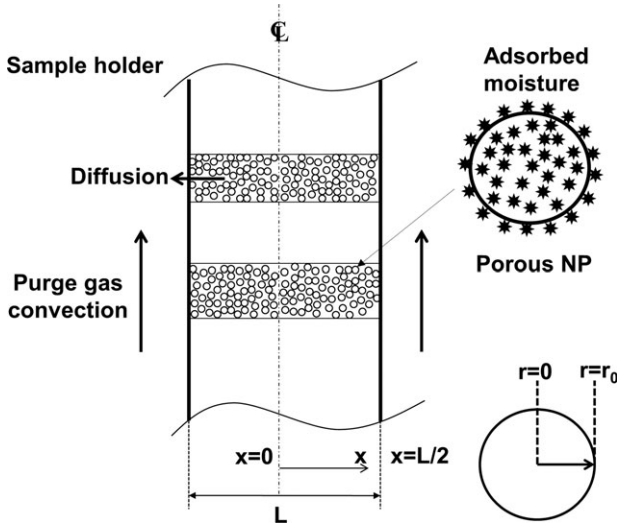

Figure 2. Schematic diagram of the NP sample holder.

The total adsorption and desorption energy are

$$E_a = E_{a_1}\frac{C_{s_{in,0}} - C_{s_{in}}}{C_{s_{in,0}}} + E_{a_2}\frac{C_{s_{in}}}{C_{s_{in,0}}}, \tag{5}$$

$$E_d = E_{d_1}\frac{C_{s_{in,0}} - C_{s_{in}}}{C_{s_{in,0}}} + E_{d_2}\frac{C_{s_{in}}}{C_{s_{in,0}}}, \tag{6}$$

where E_{a_1} and E_{d_1} are the total adsorption and desorption energy for chemisorption; and are the total adsorption and desorption energy for physisorption, and $C_{s_{in,0}}$ is the saturated moisture concentration on the total adsorbed surface, which is the initial surface concentration for the purge phase.

In Eqs. 5 and 6, total energies of adsorption and desorption are decided by sum of the chemisorption energy and physisorption energy multiplied by a weight factor. The weight factor is associated with the surface concentration and the saturated surface concentration. The total adsorption and desorption energy for chemisorption are related to the total number of available sites on the NP substrate. For instance, E_{a_1} is the sum of adsorption energy of each chemisorbed site on the NP substrate. The total adsorption and desorption energy for physisorption are determined by the total number of physisorbed molecules in equilibrium with a certain challenge concentration. It is due to the fact that different challenge concentrations vary the number of adsorbed layers, and give different number of physisorbed molecules on the surface. Therefore, all these energies may vary with different NP species or same NP species with different sizes.

In the beginning of the purge phase, the sample is fully saturated. Most of the desorbed water molecules are formed by physisorption. As $C_{s_{in}}$ is equal to $C_{s_{in},0}$ at the saturated point, it is the physisorption energy that dominates in Eqs. 5 and 6. As long as the $C_{s_{in}}$ decreases during the purge phase, the weight factor of chemisorption in Eqs. 5 and 6 will increase constantly. During the late purge phase, most of the physisorbed water molecules have been purged, and the chemisorption energy will dominate the total adsorption and desorption energy.

As shown in Figure 2, the purging gas flows along both sides of the packed-bed coupon, so the water molecules can only interact with the NPs by diffusion. L is the thickness of

the packed-bed coupon. Since the geometry is symmetric, the model has been applied to one half of the coupon.

The conservation equation of moisture in the gas phase can be presented as

$$\frac{\partial C_{g_{in}}}{\partial t} = D_{e_{in}} \frac{1}{r^2} \frac{\partial}{\partial r}\left(r^2 \frac{\partial C_{g_{in}}}{\partial r}\right) + \left[k_d C_{s_{in}} - k_a C_{g_{in}}(S_0 - C_{s_{in}})\right] \frac{A_s}{V}, \tag{7}$$

where $C_{g_{in}}$ is the moisture concentration in the gas phase, $D_{e_{in}}$ is the effective diffusivity inside of the NP domain, A_s is the total surface area of one single NP, V is the solid volume of one porous NP, and r is the radius of NPs.

The effective diffusion coefficient in a porous medium inside of the NP domain is function of free molecular diffusion coefficient and physical properties of the solid matrix, which is given by

$$D_{e_{in}} = D_A \varepsilon_{in}^2, \tag{8}$$

where D_A is the molecular diffusion coefficient of the water molecule in the nitrogen gas, ε_{in} is the porosity of one single NP, and it assumes all the NPs have the same porosity.

The conservation equation for moisture concentration on the surface of NPs is

$$\frac{\partial C_{s_{in}}}{\partial t} = k_a C_{g_{in}}(S_0 - C_{s_{in}}) - k_d C_{s_{in}}, \tag{9}$$

where $C_{s_{in}}$ is an implicit function of x given by Eq. 7.

Initial conditions for the conservation equations of $C_{g_{in}}$ and $C_{s_{in}}$ are

$$t = 0, \quad C_{g_{in}} = C_{g_{in,0}}, \tag{10}$$

$$t = 0, \quad C_{s_{in}} = C_{g_{in,0}}, \tag{11}$$

where $C_{g_{in,0}}$ and $C_{s_{in,0}}$ are the initial moisture concentration in the gas phase and on the surface of NPs, respectively. $C_{g_{in,0}}$ is always 0.1 g mol/m^3 for each challenge phase. $C_{s_{in,0}}$ depends on surface properties of NPs, and it is determined by the saturation point from the experimental data.

Boundary conditions

$$r = 0, \quad \frac{\partial C_{g_{in}}}{\partial r} = 0, \tag{12}$$

$$r = r_0, \quad -D_{e_{in}} \frac{\partial C_{g_{in}}}{\partial r} = k_m\left(C_{g_{out}} - C_{g_{in}}\right), \tag{13}$$

where r_0 is the radius of NP, which depends on the different sizes of NP samples, k_m is the NP surface mass-transfer coefficient, $C_{g_{out}}$ is moisture concentration in the gas phase outside of the NP, which is in the packed-bed domain.

k_a, k_d and S_0 should follow the relationship of equilibrium when the sample gets saturated, which is

$$k_{a,t=0} C_{g_{in,0}}\left(S_0 - C_{s_{in,0}}\right) = k_{d,t=0} C_{g_{in,0}}, \tag{14}$$

$$k_{a,t=0} = k_{a_0} \exp\left(\frac{-E_{a_2}}{RT}\right), \tag{15}$$

$$k_{d,t=0} = k_{d_0} \exp\left(\frac{-E_{d_2}}{RT}\right), \tag{16}$$

Packed-bed domain

In the multiple particle packed-bed domain, the conservation equation of moisture in the gas phase is shown below as

$$\frac{\partial C_{g_{out}}}{\partial t} = D_{e_{out}} \frac{\partial^2 C_{g_{out}}}{\partial x^2} - D_{e_{in}} \frac{\partial C_{g_{in}}}{\partial r}\bigg|_{r=r_0} 4\pi r_0^2 N_v, \tag{17}$$

where $D_{e_{out}}$ is the effective diffusivity in the packed-bed domain, and N_v is the number of NPs per unit volume in the packed-bed.

The number of NPs per unit volume of the packed-bed can be defined as

$$N_v = \frac{m}{\rho \frac{4}{3}\pi r^3 (1 - \varepsilon_{in}) V_b} \tag{18}$$

where m is the total mass of NP sample, ρ is the density of NP sample, and V_b is the volume of the packed-bed.

During the purge phase, moisture in the gas phase inside of the packed-bed domain is accumulated from each NP domain by diffusion. In the packed-bed domain, moisture diffuses to the boundary between the packed-bed and the purge gas, and is purged by mass transport.

The effective diffusion coefficient in the packed-bed domain is function of free molecular diffusion coefficient and physical properties of the solid matrix, which is similar as Eq. 8.

Initial condition for the conservation equations of $C_{g_{out}}$ is

$$t = 0, \quad C_{g_{out}} = C_{g_{out,0}}, \tag{19}$$

where $C_{g_{out,0}}$ is the initial moisture concentration in the gas phase of packed-bed.

Boundary conditions are

$$x = 0, \quad \frac{\partial C_{g_{out}}}{\partial x} = 0, \tag{20}$$

$$x = \frac{L}{2}, \quad D_{e_{out}} \frac{\partial C_{g_{out}}}{\partial x} = k_m C_{g_{out}}. \tag{21}$$

where L is the thickness of the packed-bed.

Relationship between absorbance and surface concentration

In order to convert the integral of absorbance peak over wave number to the surface concentration, Beer's law has been introduced to establish the relationship between these two.

Following the Beer's law, the surface concentration is integrated from the initial point to the final point as follows

$$\int_{I_0}^{I_f} \frac{dI}{I} = -\frac{a}{r_0} \int_0^L \int_0^{r_0} C_{s_{in}}(r, x, t) dr dx), \tag{22}$$

where I is the intensity of the light, α is the molar absorptivity, r_0 is the radius of NP and I_0, I_f are the intensity (or power) of the incident light and the transmitted light, respectively.

The absorbance A is given by

$$A = \int_{I_0}^{I_f} \frac{dI}{I} = -\frac{\ln I_f}{I_0}. \tag{23}$$

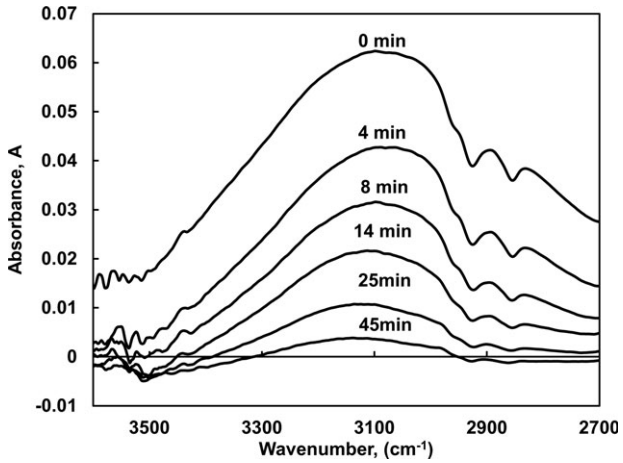

Figure 3. FTIR spectra of 20 nm SiO_2 at 55°C at different times during the purge process.

Equations 22 and 23 could give the expression for absorbance A based on the integral of surface concentration

$$A = \frac{a}{r_0}\int_0^L \int_0^{r_0} C_{s_{in}}(r,x,t)drdx, \tag{24}$$

The spectra from the experimental data shows the plot of absorbance with respect to wave number λ, and the integral of absorbance peak over wave number could be integrated by FTIR software. Since $C_{s_{in}}$ is not a function of λ, the integral of absorbance peak over wave number A_{int} is

$$A_{\text{int}} = \int_{\lambda_1}^{\lambda_2} Ad\lambda = \frac{a}{r_0}\int_{\lambda_1}^{\lambda_2} ad\lambda \int_0^L \int_0^{r_0} C_{s_{in}}(r,x,t)drdx. \tag{25}$$

where λ_1 and λ_2 are the initial and final wave numbers of the absorbance peak, respectively.

As the range of absorbance peak wave number is maintained for all the samples, the integral of absorbance peak over wave number has a linear relationship with the double integral of $C_{s_{in}}$ over x and r.

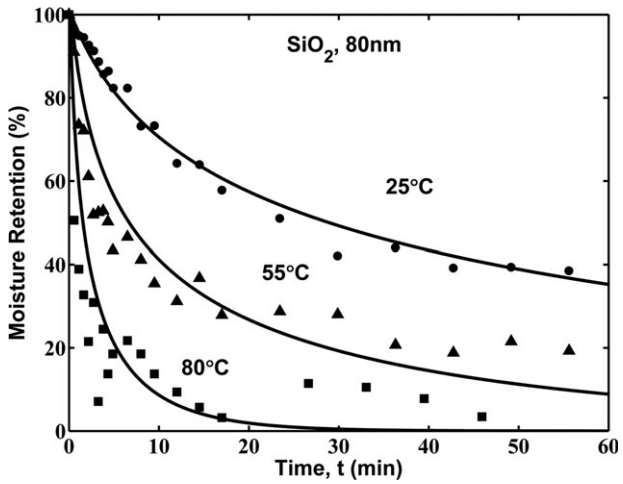

Figure 4. Experimental and modeling results for moisture desorption from 80 nm SiO_2 NPs at various temperatures (modeling results are based on Table 1 parameters).

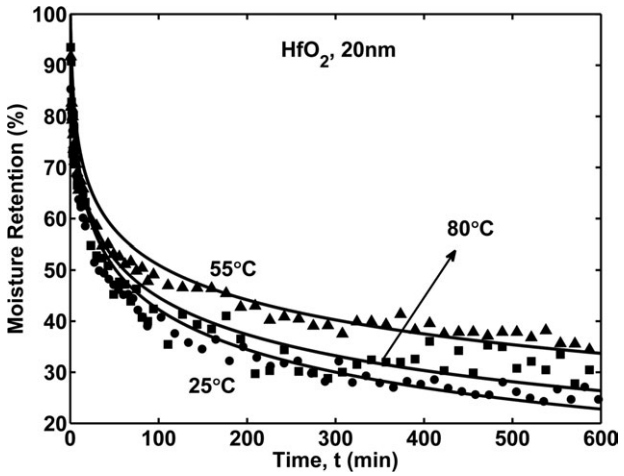

Figure 5. Experimental and modeling results for moisture desorption from 20 nm HfO_2 NPs at various temperatures (modeling results are based on Table 2 parameters.)

Using Eq. 25, the integral of absorbance peak over wave number has been transferred into moisture retention percentage M as below

$$M = \frac{A_{int}}{A_{int,t=0}} \times 100, \tag{26}$$

where $A_{\text{int},t=0}$ is the initial integral of absorbance peak over wave number.

Results and Discussion

Analysis of FTIR spectra

Water molecules contain three different modes of vibration: symmetric stretch (v_1), asymmetric stretch (v_3), and bending (v_2). Hydrogen bonding could influence the peak shape and intensity; it could generally cause peak broadening and shifts in absorption to lower frequencies.[12] Usually, the main stretching band of water vapor is around 3,800 cm^{-1} (asymmetric stretch, 3,756 cm^{-1} and symmetric stretch, 3,657 cm^{-1}). The spectra contains a mass of sharp peaks around that frequency which is related to the water in the gas phase. Because of hydrogen bonding, the liquid water stretch vibration is shifted to a lower frequency (asymmetric stretch, 3,490 cm^{-1} and symmetric stretch, 3280 cm^{-1}).[13] The bending frequency increases (bending v_2, 1,644 cm^{-1}) because of the hydrogen bonding.[14]

Figure 3 shows the spectrum change from SiO_2 saturated sample to clean sample as time goes on in the purge stage. There is a group of sharp peaks around the 3,800 cm^{-1} which represent water vapor stretching frequency. The broader absorption peak from 3,500 cm^{-1} to 2,700 cm^{-1} refers to main stretching band of liquid water. Compared with the stretching frequency of water vapor, the main stretching band of liquid water has been shifted to a lower frequency by hydrogen bonding. All the NP samples in this study contain this broad absorption peak; therefore, this peak is used to measure the moisture concentration on the surface of NPs.

In addition, the broader absorption peak from 3,500 cm^{-1} to 2,700 cm^{-1} also means there is condensed water among NPs. This is because of capillary condensation (Kelvin effect), which is due to an increased number of van der

Table 1. Saturated Surface Concentration, Fractional Coverage on Exposure to 0.1 g mol·m^{-3} Moisture, and Adsorption and Desorption Kinetic Parameters of 20 nm and 80 nm SiO_2 NPs at Various Temperatures

Sample	Saturated surface concentration C_{S_0} (gmol·m^{-2})	Fractional coverage θ (%)	E_{a_1} (kJ·gmol^{-1})	E_{a_2} (kJ·gmol^{-1})	E_{d_1} (kJ·gmol^{-1})	E_{d_2} (kJ·gmol^{-1})
SiO_2 (20 nm), 25°C	2.0×10^{-6}	67	9.0	6.0	16.0	12.5
SiO_2 (20 nm), 55°C	1.9×10^{-6}	63	9.0	1.2	13.0	8.0
SiO_2 (20 nm), 80°C	1.5×10^{-6}	50	9.0	0.1	7.6	5.7
SiO_2 (80 nm), 25°C	1.1×10^{-6}	37	10.0	6.5	15.5	10.0
SiO_2 (80 nm), 55°C	1.0×10^{-6}	33	10.0	2.0	12.5	5.5
SiO_2 (80 nm), 80°C	5.3×10^{-7}	18	10.0	1.0	7.5	2.2

Waals interactions between water vapor molecules inside the confined space of a capillary. The condensed water is formed between NPs where water vapor condensation occurs below the saturation water vapor pressure.

Based on the previous study, water molecules begin to adsorb on the surface of NPs such as SiO_2, CeO_2 and HfO_2, and splits into two parts: one is hydrogen bond and the other is hydroxyl bond. For SiO_2, one siloxane bond is opened and a hydroxyl bond is attached to the silicon molecule. At the same time a hydrogen bond attaches to the oxygen molecule on the other siloxane bond.[10] CeO_2 and HfO_2 share the same bond-breaking mechanism when water molecules adsorb on the surface of these two NPs. It is chemisorption that happens between the the first layer adsorbate and substrate. After the first layer has been partially formed, water molecules will keep adsorbing on water molecules attached to the substrate, which is called physisorption. This will generate the hydrogen bonding in each physisorbed layer and contribute to shifting the stretching band of water molecules to lower frequency. The result is a broader absorption peak from 3,500 cm^{-1} to 2,700 cm^{-1}, which is lower than the characteristic stretching frequency of water vapor.

During the purge process, immediately after the switch to purge phase, the disappearance of the main sharp stretching band of water vapor around 3,800 cm^{-1} indicates that most of the moisture in the bulk flow was removed after switching to purge phase.[10] As Eq. 25 shows, the measured absorbance peak only corresponds to the surface concentration of moisture on the NP surface area.

Since the desorption rate is much higher than the adsorption rate during the purge phase, water molecules that desorb from the surface diffuse to the boundary between bulk flow and surface of the coupon. The water molecules are then transferred to the bulk gas and are carried away by UHP N_2. The broad peak from 3,500 cm^{-1} to 2,700 cm^{-1} keeps decreasing with time as shown in Figure 3. As the contribution from water vapor is negligible, the integral of absorbance peak over wave number from 3,500 cm^{-1} to 2,700 cm^{-1} corresponds to the moisture concentration on the surface of NPs. Since the range of wave numbers is maintained for all the sample, the integral of absorptivity over λ is a constant in Eq. 25. The integral of absorbance peak over wave number has a linear relationship with the double integral of moisture surface concentration over x and r.

Model verification

Figures 4 and 5 show the comparison of model results with the experimental data for SiO_2 (80 nm) and HfO_2 (20 nm) at three different temperatures. The scatter in experimental data increases at low-surface concentrations because of the limitations of the analyzer. Similar results were obtained for SiO_2 (20 nm), CeO_2 (20 nm, 50 nm), and HfO_2 (100 nm) at different temperatures. For the model predictions, the porosity of the packed-bed, randomly packed, and the intraphase porosity of NPs particles are both assumed to be 0.3 for all the NP samples. The molecular diffusivity of moisture in the nitrogen delivery gas is equal to 2.6×10^{-5}; $m^2 \cdot s^{-1}$; the effective diffusion coefficients inside the NPs and in the packed-bed vary with the porosity of the packing bed and the porosity of NPs, according to Eq. 8; the relationship between the integral of absorbance peak over wave number and the double integral of surface concentration is determined by the initial point of each experimental data, using Eq. 25. Therefore, k_m, k_a and k_d remain as the only unknown parameters determined by fitting the model to the experimental data. On a relative basis, k_a and k_d are the most critical fitting parameters for the data fitting. Based on Eqs. 3 to 6, the total activation energies and the pre-exponential factors for adsorption and desorption rate coefficients are fit parameters for the model configuration. Therefore, there are seven adjustable fitting parameters in the process model $k_{a_0}, k_{d_0}, E_{a_1}, E_{a_2}, E_{d_1}, E_{d_2}$ and k_m. Since maximum capacity S_0 is only related to the material and the prefactor and are not the functions of temperature, they all remain the same for the same type of NPs at different temperatures. The experimental data profiles that are being fitted include a large number of points over a wide range of conditions. This "profile fitting" is selective and discriminating and highly

Table 2. Saturated Surface Concentration, Fractional Coverage on Exposure to 0.1 g mol·m^{-3} Moisture, and Adsorption and Desorption Kinetic Parameters of 20 nm and 100 nm HfO_2 NPs at Various Temperatures

Sample	Saturated surface concentration C_{S_0} (gmol·m^{-2})	Fractional coverage θ (%)	E_{a_1} (kJ·gmol^{-1})	E_{a_2} (kJ·gmol^{-1})	E_{d_1} (kJ·gmol^{-1})	E_{d_2} (kJ·gmol^{-1})
HfO_2 (20 nm), 25°C	2.2×10^{-6}	55	5.0	0.5	17.0	0.4
HfO_2 (20 nm), 55°C	1.5×10^{-6}	38	5.0	2.8	23.5	0.7
HfO_2 (20 nm), 80°C	8.1×10^{-7}	20	5.0	4.8	22.0	0.016
HfO_2 (100 nm), 25°C	4.4×10^{-7}	11	12.5	10.5	16.5	4.6
HfO_2 (100 nm), 55°C	3.3×10^{-7}	8.3	12.5	11.0	16.0	3.7
HfO_2 (100 nm), 80°C	3.1×10^{-7}	7.8	12.5	12.0	11.0	2.6

Table 3. Saturated Surface Concentration, Fractional Coverage on Exposure to 0.1 g mol·m^{-3} Moisture, and Adsorption and Desorption Kinetic Parameters of 20 nm and 50 nm CeO_2 NPs at Various Temperatures

Sample	Saturated surface concentration C_{S_0} (gmol·m^{-2})	Fractional coverage θ (%)	E_{a_1} (kJ·gmol^{-1})	E_{a_2} (kJ·gmol^{-1})	E_{d_1} (kJ·gmol^{-1})	E_{d_2} (kJ·gmol^{-1})
CeO_2 (20 nm), 25°C	8.3×10^{-7}	10.4	1.9	1.5	46	7.8
CeO_2 (20 nm), 55°C	8.2×10^{-7}	10.3	1.9	1.2	30	8.1
CeO_2 (20 nm), 105°C	8.1×10^{-7}	10.1	1.9	1.0	10	8.9
CeO_2 (50 nm), 25°C	5.5×10^{-7}	6.9	3.0	0.1	19	5.3
CeO_2 (50 nm), 55°C	3.7×10^{-7}	4.6	3.0	0.1	20	4.7
CeO_2 (50 nm), 105°C	3.6×10^{-8}	4.5	3.0	0.1	9	5.0

sensitive to variations in the parameters compared to fitting to a few experimental data points. So, the experimental results could not be fitted to multiple sets of parameters. Least-squares regression has been applied to determine the best fit to the data. Tables 1 through 4 show the value of the process parameters obtained by this analysis. Since the interaction between the substrate and the adsorbate in the first-layer (chemisorption) is stronger than that in the upper layers (physisorption), the activation energy for chemisorption is usually higher than that for physisorption. Furthermore, first-layer activation energy for desorption is usually higher than that for adsorption. Therefore, E_{a1} is larger than E_{a2} and E_{d1} is larger than E_{d2}. Additionally, for most cases, E_{a1} is smaller than E_{d1}.

Effect of particle size on surface characteristics

The effect of particle size on the dynamics of the adsorption and desorption process has been studied using a combination of experiments and model applications at different temperature. In Tables 1, 2 and 3, the key NP properties are compared for two different sizes of SiO_2, CeO_2 and HfO_2 at different temperatures. Fractional coverage is a measure of the fractions of maximum capacity of the surface that is occupied when the sample comes to equilibrium with a certain moisture challenge level. This is an indication of the balance between adsorption and desorption kinetics at the point of saturation. At the same challenge gas concentration, SiO_2, CeO_2 and HfO_2 at 25 have the highest saturated surface concentration and fractional coverage. Therefore, less water absorbs on the NP surface as temperature increases. For all temperatures, the smaller NPs have a higher saturation surface concentration. This is because smaller NPs have larger curvature, higher deviation from flat surface, larger number of active site density, and, consequently, more surface adsorbate.

Figure 6 shows the moisture desorption curves for SiO_2, CeO_2 and HfO_2 with two different sizes at the same temperature. SiO_2 with 20 nm particle size adsorbs more moisture than 80 nm SiO_2. As shown in Figure 6, the purge process is slower for smaller NPs. The results for the other two oxides at different temperatures show the same trend. Therefore, these results also confirm that smaller NPs get contaminated more easily and are decontaminated more slowly.

Table 4. Maximum Capacity on Exposure to 0.1 g mol·m^{-3} Moisture, and Adsorption and Desorption Kinetic Parameters of SiO_2, CeO_2, and HfO_2 NPs

Sample	Maximum capacity S_0 (gmol·m^{-2})	$k_{a,\,0}$ (m^3·gmol^{-1}·s^{-1})	$k_{d,\,0}$ (s^{-1})
SiO_2	3.0×10^{-6}	0.04	0.03
CeO_2	8.0×10^{-6}	0.001	0.012
HfO_2	4.0×10^{-6}	0.03	0.0025

As discussed in the modeling section, the adsorbed water molecules on different NP surfaces at any time are of two types: the molecules in the first chemisorbed layer that have direct and stronger interaction with the NP surface, and the upper physisorbed layers that have weaker interactions with each other. These two adsorbed types with two energy levels are combined to give the observed (apparent) activation energy corresponding to the surface coverage at that time. Since the coverage is a function of time and location in the bed of particles, the activation energy is also spatial dependent in the packed-bed and inside of NPs. The energies are always highest on the surface of a single NP and in the packed-bed where the coverage is the lowest and the fraction chemisorbed is highest. Theses energies are always lowest at the center of a single NP, and at the center of the packed-bed where coverage and the fraction physisorbed is the highest.

Figures 7 through 9 show the variation of adsorption and desorption activation energies for particles of three oxides with two different sizes. The composite activation energies for both adsorption and desorption are particle size and temperature-dependent. In Figure 7, for 20 nm and 100 nm SiO_2 NPs, the activation energy for adsorption (both chemisorption and physisorption) is higher for the larger particles, and the activation energy for desorption is lower for larger particles. The same trend is observed for the other two types of NPs at different temperatures. Therefore, the size-effect results indicate that the smaller particles adsorb the contaminant more easily and release or desorb it more slowly than

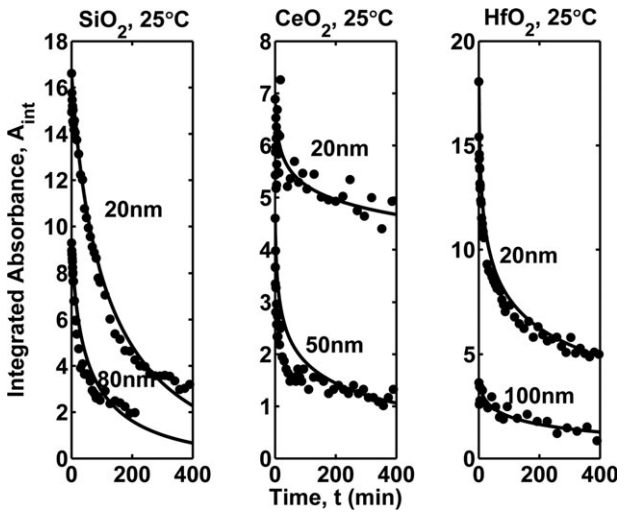

Figure 6. Time profile of moisture desorption for SiO_2, CeO_2 and HfO_2 NPs with the different sizes at 25°C (modeling results are based on Tables 1–3 parameters.)

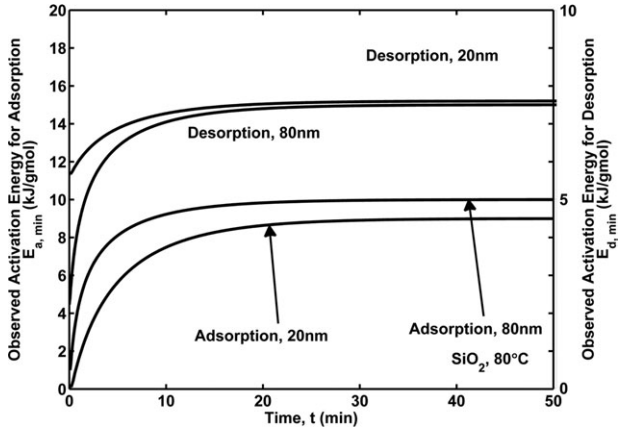

Figure 7. Observed adsorption and desorption activation energies for 20 nm and 80 nm SiO_2 NPs at 80°C.

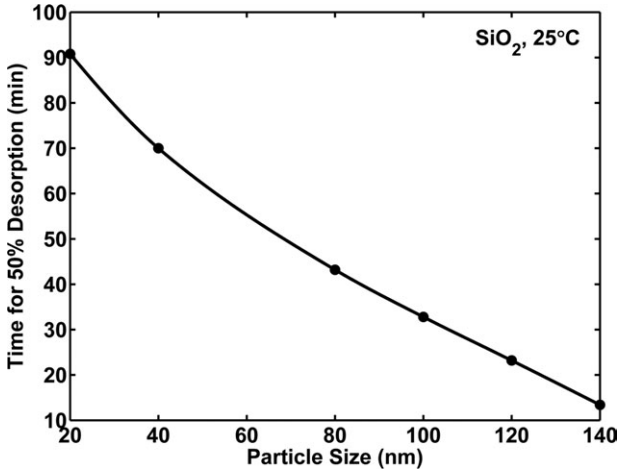

Figure 10. Time for 50% desorption for SiO_2 NPs with the different sizes at 25°C.

the larger particles based on change the activation energies trend with respect to particle size.

Figures 10 through 12 show the time required for 50% moisture removal (half-life of adsorbed moisture) with respect to the particle size predicated by the model simulation for three oxides. Figure 10 shows the time required for 50% moisture removal decreases as particle size increases for SiO_2 at 25°C. The same trend exists for CeO_2 at 55°C and HfO_2 at 25°C. Therefore, the model predications confirm that the surface properties of NPs are size-dependent and the smaller particles have higher affinity to the contaminant. The

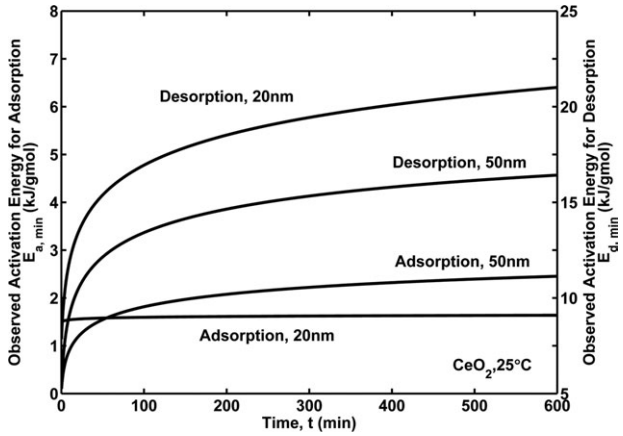

Figure 8. Observed adsorption and desorption activation energies for 20 nm and 50 nm CeO_2 NPs at 25°C.

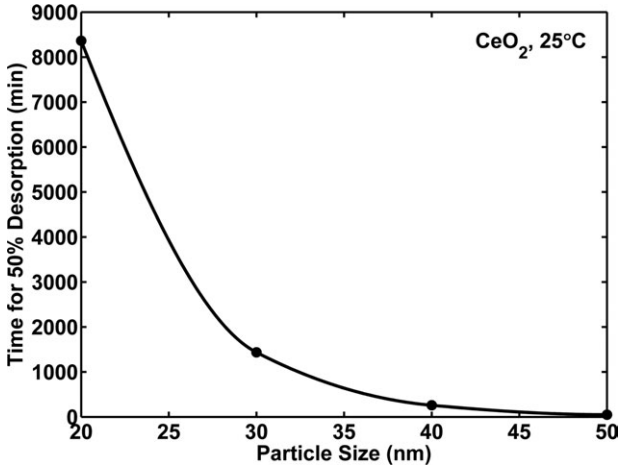

Figure 11. Time for 50% desorption for CeO_2 NPs with the different sizes at 25°C

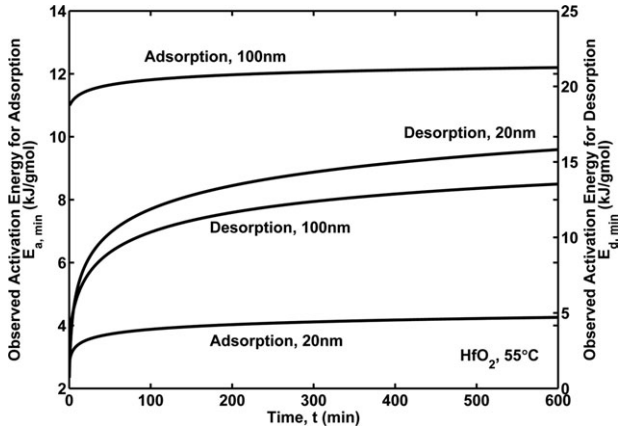

Figure 9. Observed adsorption and desorption activation energies for 20 nm and 100 nm HfO_2 NPs at 55°C.

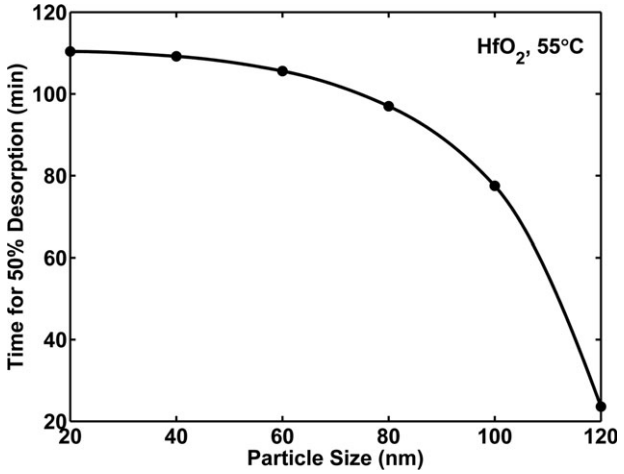

Figure 12. Time for 50% desorption for HfO_2 NPs with the different sizes at 55°C.

strong interaction with adsorbing contaminants is a key characteristic that makes NPs different from larger particles and contributes to their potential environmental and health impact.

Conclusions

A methodology consisting of combined experimental and process simulation for studying the surface characteristics of NPs at several temperatures has been developed. In this study, the method is applied to HfO_2, SiO_2, and CeO_2 nanoparticles. Moisture adsorption/desorption on these NPs is used as a way of characterizing the surface properties that affect the capture and the retention of homogeneous contaminants on NP surfaces. The method consists of *in situ* FTIR for obtaining the dynamics of interaction between adsorbate and NP surfaces at different temperatures. A process simulator is developed that is useful in determining the fundamental NP surface properties. The results indicate that as particle size decreases, NPs are more prone to contamination and harder to decontaminate once the contaminant adsorption has taken place. The enhancement of the adsorption process with the decrease in particle size is expected to be a major contributor to the enhanced environmental and health impact of NPs compared to that of larger particles.

Acknowledgment

This study is a part of the program of the SRC/Sematech Engineering Research Center for Environmentally Benign Semiconductor Manufacturing (CEBSM). The authors acknowledge financial support from SRC, Sematech, and other members of the CEBSM.

Notation

A = absorbance
a = molar absorptivity, m/mol
A_{int} = integrated absorbance over wave number, m^{-1}
A_s = total surface area of one single NP, m^2
C_{gin} = gas phase moisture concentration in NP domain, g mol·m^{-3}
$C_{gin,0}$ = initial gas phase moisture concentration in NP domain, g mol·m^{-3}
C_{gout} = gas phase moisture concentration in packed-bed domain, g mol·m^{-3}
$C_{gout,0}$ = initial gas phase moisture concentration in packed-bed domain, g mol·m^{-3}
C_{sin} = surface moisture concentration in NP domain, g mol·m^{-2}
$C_{sin,0}$ = saturated surface concentration in NP domain, g mol·m^{-2}
D_A = molecular diffusion coefficient, m^2·s^{-1}
D_{ein} = effective diffusivity in NP domain, m^2·s^{-1}
D_{eout} = effective diffusivity in packed-bed domain, m^2·s^{-1}
E_a = activation energy of adsorption, kJ·g mol^{-1}
E_{a1} = intrinsic adsorption energy for chemisorption, kJ·g mol^{-1}
E_{a2} = intrinsic adsorption energy for physisorption, kJ·g mol^{-1}
E_d = activation energy of desorption, kJ·g mol^{-1}
E_{d1} = intrinsic desorption energy for chemisorption, kJ·g mol^{-1}
E_{d2} = intrinsic desorption energy for physisorption, kJ·g mol^{-1}
I = intensity of the light
I_0 = intensity of incident light
I_f = intensity of transmitted light
k_a = adsorption rate coefficient, m^3·g mol^{-1}·s^{-1}
k_{a0} = pre-exponential factors for adsorption, m^3·g mol^{-1}·s^{-1}
$k_{a,t=0}$ = adsorption rate coefficient at $t = 0$, m^3·g mol^{-1}·s^{-1}
k_d = desorption rate coefficient, s^{-1}
k_{d0} = pre-exponential factors for desorption, s^{-1}
$k_{d,t=0}$ = desorption rate coefficients at $t = 0$, s^{-1}
k_m = surface mass-transfer coefficient in NP and packed-bed domain, m·s^{-1}
L = thickness of packed-bed, m
m = total mass of NP sample, kg
N_v = number of NPs per unit volume in the packed-bed, m^{-3}
R = gas constant, kJ·g mol^{-1}·K^{-1}
r = position along the radius of one NP, m
r_0 = radius of nanoparticle, m
r_a = adsorption rate, g mol·m^{-2}·s^{-1}
r_d = desorption rate, g mol·m^{-2}·s^{-1}
S_0 = maximum capacity of the surface, g mol·m^{-2}
T = temperature, K
t = time, s
V = solid volume of one porous NP, m^3
V_s = volume of packed-bed, m^3
x = position along the thickness of the packed-bed, m

Greek alphabet

ε_{in} = NP porosity
λ = wave number, m^{-1}
ρ = the density of NP sample, kg/m^3

Abbreviations

APIMS = atmospheric pressure ionization mass spectrometer
CRDS = cavity ring-down spectrometer
ESH = environmental safety and health
FTIR = Fourier transform infrared
IR = infrared
MFC = mass flow controller
NP = nanoparticle
ppm = parts per million
UHP = ultra high purity

Literature Cited

1. Hudson SP, Padera RF, Langer R, Kohane DS. The biocompatibility of mesoporous silicates. *Biomater*. 2008;29:4045–4055.
2. Slowing I, Trewyn BG, Lin VS, Effect of surface functionalization of MCM-41-Tpye mesoporous silica nanoparticles on the endocytosis by human cancer cells. *J Am Chem Soc*. 2006;128:14792–14793.
3. Nguyen TPB, Lee JW, Shim WG, Moon H. Synthesis of functionalized SBA-15 with ordered large pore size and its adsorption properties of BSA. *Microporous Mesoporous Mater*. 2008;110: 560–569.
4. Maurer-Jones MA, Lin YS, Haynes CL. Functional assessment of metal oxide nanoparticle toxicity in immune cells. *ACS Nano*. 2010;4:3363–3373.
5. Mawhiney DB, Rossin JA, Gerhart K, Yates JT Jr. Adsorption studies by transmission IR spectroscopy: a new method for opaque materials. *Langmuir*. 1999;15:4617.
6. Karge HG, Nießen WA. New method for the study of diffusion and counter-diffusion in zeolite. *Catal Today*. 1991;8:451.
7. Hunger B, Heuchel M, Matysik S, Beck K, Einicke WD. Adsorption of water on ZSM-5 zeolites. *Thermochimica Acta*. 1995;269/270:599–611.
8. Rege SU, Yang RT. A novel FTIR method for studying mixed gas adsorption at low concentrations: H_2O and CO_2 on NaX zeolite and γ-alumina. *Chem Eng Sci*. 2001;56:3781–3796.
9. Dillon AC, Gupta P, Robinson MB, Bracker AS, George SM. FTIR studies of water and ammonia decomposition on silicon surfaces. *J Electron Spectrosc*. 1990;54/55:1085–1095.
10. Wang H, Yao J, Shadman F. Characterization of the surface properties of nanoparticles using moisture adsorption dynamic profiling. *Chem Eng Sci*. 2011;66(12):2545–2553.
11. Desjonquères MC, Spanjaard D. *Concepts in Surface Physics*. Berlin, Germany: Springer-Verlag; 1993.
12. Settle FA. *Handbook of Instrumental Techniques for Analytical Chemistry*. Upper Saddle River, NJ: Prentice Hall; 1997.
13. Eisenberg D, Kauzmann W. *The Structure and Properties of Water*. 1st ed. New York, NY: Oxford University Press; 1969.
14. Max J-J, Chapados C. Isotope effects in liquid water by infrared spectroscopy. III. H_2O and D_2O spectra from 6000 to 0 cm^{-1}. *J Chem Phys*. 2009;131(18):184505.

Manuscript received July 18, 2011, and revision received Sept. 18, 2012.